The San Andreas Fault revisited through seismic-noise and surface-wave tomography

Philippe Roux, Marc Wathelet, Antoine Roueff

The San Andreas Fault revisited through seismic-noise and surface-wave tomography

Philippe Roux,[1] Marc Wathelet,[1] and Antoine Roueff[2]

Received 15 April 2011; revised 23 May 2011; accepted 24 May 2011; published 15 July 2011.

[1] We present here surface-wave tomography results for the San Andreas Fault in the Parkfield area, California, USA, that were extracted from microseismic noise in the 0.15 Hz to 0.35 Hz frequency band using passive seismic-correlation techniques. Using directive noise incoming from the Pacific Ocean, passive seismic-noise tomography was performed using three-component sensors from a dense seismic network. A rotation algorithm was applied to the nine-component noise-correlation tensor that optimally forced each station pair to re-align in the noise direction, a necessary condition to extract unbiased travel-times from passive seismic processing. After the rotation was performed, an optimal surface-wave tensor is obtained from which Love waves were extracted for tomography inversion. Dispersion curves were then inverted to obtain a three-dimensional shear-velocity map showing vertical geological structures and a 1.3-km wide low seismic velocity dip, which are in agreement with previous tomography studies in the same area. **Citation:** Roux, P., M. Wathelet, and A. Roueff (2011), The San Andreas Fault revisited through seismic-noise and surface-wave tomography, *Geophys. Res. Lett.*, *38*, L13319, doi:10.1029/2011GL047811.

1. Introduction

[2] Surface-wave tomography has traditionally exploited the frequency-dependent wave-velocity characteristics of Rayleigh and Love waves. Surface waves sample the earth structure to a given depth, with higher frequencies sampling shallower structures. In recent years, surface-wave tomography results have been obtained through correlation of ambient seismic noise [*Sabra et al.*, 2005; *Shapiro et al.*, 2005]. Indeed, the resulting signals after cross-correlation of long time records at two stations were dominated by surface waves, since the background seismic noise mainly consisted of surface waves at the free surface of the Earth. Tomography results with seismic noise often provide high-resolution group-velocity maps for Rayleigh waves within the 5-s to 50-s period band, on distances ranging from 50 km to 5,000 km [*Moschetti et al.*, 2007; *Yang et al.*, 2007; *Bensen et al.*, 2007]. What makes ambient-noise surface-wave tomography (ANSWT) appealing is that its spatial resolution only depends on the density of the seismic stations on which the noise correlation is performed. In other words, the spatial resolution of ANSWT can be controlled *a priori* by choosing the number and locations of the seismic stations on which the noise is recorded.

[3] This makes a big difference with surface-wave dispersion measurements that are performed along earthquake-to-station paths [*Ekström et al.*, 1997], which often suffer from non-uniformity of the spatial distribution of the earthquake sources. For example, through one year of seismic noise records, a three-dimensional (3-D) view of the Moho depth was obtained in the Alpine region [*Stehly et al.*, 2009] that surpassed the resolution of an equivalent map obtained from the accumulation of both earthquake tomography and seismological studies using controlled sources [*Waldhauser et al.*, 1998]. On the other hand, *Stehly et al.* [2009] also showed that the resolution of seismic-noise tomography can be limited by the spatial distribution of the noise sources, which might not be uniform in the frequency bandwidth of interest, even when considering long time-series or additional randomisation produced by scattering on small-scale heterogeneities within the Earth. Indeed, one theoretical ingredient for ANSWT to succeed is an azimuthally uniform distribution of noise sources around the seismic network, which is never the case in practice. Methodological aspects and potential bias associated with the spatial distribution of the noise have been studied recently for seismic-noise tomography [*Yao and Van der Hilst*, 2009; *Froment et al.*, 2010].

[4] *Roux* [2009] recently presented surface-wave tomography results based on noise correlation for both Rayleigh and Love waves in the unfavourable case of directive ambient seismic noise. The data were taken among the nearby stations deployed in the Parkfield area. To take advantage of the largest number of station pairs in the ANSWT, an Optimal Rotation Algorithm (ORA) was applied to each station pair, to provide unbiased travel-time measurements for both Rayleigh and Love waves. In practice, the ORA manipulated the noise-correlation tensor by allowing each station to freely turn around both the vertical and radial directions. Assuming that the Z, R and T indices corresponded to the vertical, radial and transverse components of each station, the optimal rotation angles were those which minimised the total energy on the transverse components ZT, TZ, RT and TR of the correlation tensor. For each station pair, the ORA then provided an optimal noise correlation tensor with the Rayleigh wave on the new ZZ, ZR, RZ and RR components, and the Love wave on the new TT component. The decomposition of the noise correlation tensor into its surface-wave components can instead be performed using intrinsic coherence and polarisation filtering [*Roueff et al.*, 2009]. This second method does not assume *a priori* that waves are polarized in orthogonal directions and provides a validation of the results obtained by the ORA.

[1] ISTerre, CNRS, IRD, Université Joseph Fourier, Grenoble, France.
[2] Institut Fresnel, CNRS, Aix-Marseille Université, Ecole Centrale Marseille, Marseille, France.

0094-8276/11/2011GL047811

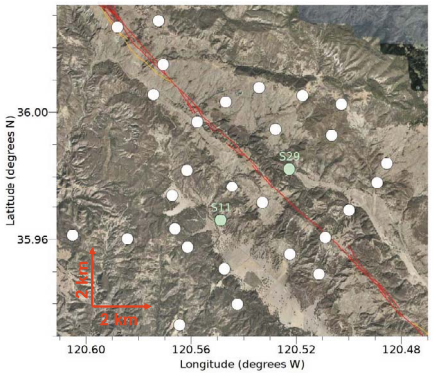

Figure 1. Topographic map of the Parkfield area (an 11 km square; California, USA) showing the San Andreas Fault (red) and the 30 seismic stations (circles) deployed temporarily in the Parkfield area between July 2001 and October 2002.

[5] Using ANSWT for Love waves only, this study presents a 3-D shear-wave velocity map of the San Andreas Fault (SAF) in Parkfield, California, USA. The choice of Love waves for this inversion was motivated by (1) their high sensitivity to shallow geophysical structure and (2) the residual pollution of P-waves on the ZZ and RR components [*Roux et al.*, 2005] that may bias the dispersion curve of Rayleigh waves.

[6] ANSWT appears to be an alternative to the short-distance P-wave tomography that is classically performed in the area from reflection/refraction seismic active experiments and/or travel-times obtained from local earthquakes.

2. Data Analysis and Tomography

[7] The tomography results arose from the seismic ambient noise recorded on a dense temporary seismic network deployed in the Parkfield area between July 2001 and October 2002 (Figure 1) [*Thurber et al.*, 2004]. As ambient seismic noise is strongly dominated by the secondary peak microseism excitation incoming from the Pacific Ocean [*Tanimoto et al.*, 2006], the 3-component signals were pre-whitened in the 2.5 s to 18 s period band on each of the 30 broadband stations, to extend the group velocity analysis to higher frequencies. Only 15 days of continuous recording were necessary to obtain strong spatial coherence between all of the station pairs.

[8] For each of the station pairs, the ORA transformed the nine-component noise-correlation tensor into a surface-wave's tensor that projected along the incoming noise direction. Beamforming results performed on the ambient noise data showed that the noise field clearly originated from the Pacific Ocean (incidence angle, $\theta_0 \sim 55°$; North is 0°, positive rotation is clockwise), with small daily fluctuations that correlated with significant wave heights measured along the Californian shore. Despite the short distances between the stations, no near-field contributions of the surface-wave's function were retrieved from the noise correlation, as the dominant noise source was in the far field. This confirms that noise correlation on long time records simply behaves as a time-domain interferometer that magnifies phase coherence between station pairs in the frequency bandwidth of interest.

[9] Among the 435 noise-correlation tensors obtained for each of the station pairs, the ORA extracted more than 360 surface-wave tensors that re-aligned correctly along the noise direction and provided unambiguous identification of the Love wave contributions. Intrinsic coherence and polarization filtering method confirmed these results. The rejected noise-correlation tensors mainly corresponded to the station pairs with both stations located very close to the SAF, for which the noise correlation appeared to be dominated by trapped waves along the fault [*Li et al.*, 2004]. From the collection of Love broadband traces, the travel-times were extracted for group velocity inversions on a subset of frequencies, *Fc*, ranging from 0.15 Hz to 0.35 Hz (Figure 2).

[10] For tomography purposes, we made the arbitrary choice to attribute each travel-time to an effective distance, defined as the station-pair mid-path projected along the noise direction. Elevation of the stations was not considered. At each frequency *Fc*, a simple linear inversion was performed on the arrival-time residuals, to construct the tomographic map [*Barmin et al.*, 2001]. Here we assumed straight rays as propagation paths and an *a-priori* error covariance matrix that decreased exponentially with distance over 2.5 km. The weight of the spatial smoothing was chosen at the maximum curvature of the standard trade-off (L-curve) analysis, based on the misfit value. We used a homogeneous starting model (independent of frequency) with group velocities of c_{0L} = 2.2 km/s for the Love wave (Figure 2). At each

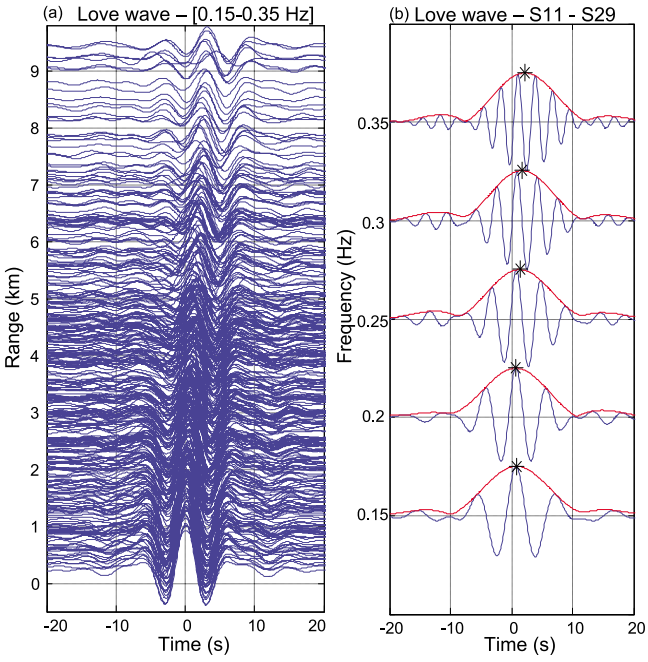

Figure 2. (a) Range *versus* time correlation functions corresponding to the Love waves after the Optimal Rotation Algorithm was applied to each noise correlation tensor. The average group speed for Love wave was c_{0L} = 2.2 km/s. (b) The group-velocity dispersion curve of the Love wave is extracted from the TT component (blue) of each surface-wave tensor (here the station pair S11–S29). The black stars correspond to the travel-time measurement for group velocity (red) at each frequency. Stations S11 and S29 are displayed in Figure 1.

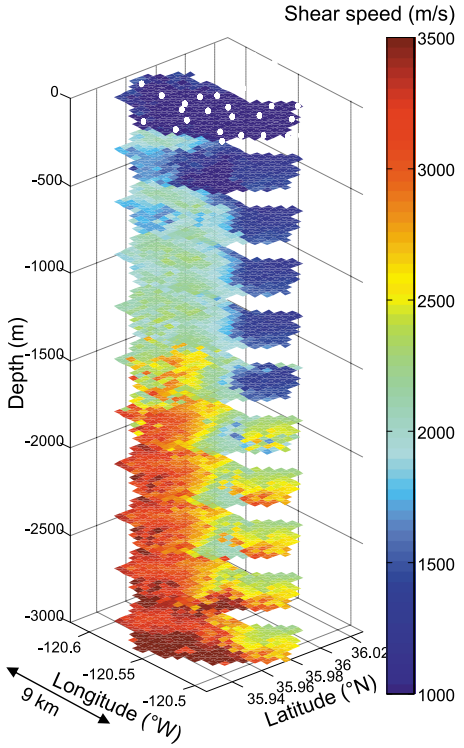

Figure 3. Three-dimensional shear-wave velocity map around the San Andreas Fault obtained from the Love wave dispersion curves in the 0.15 Hz to 0.35 Hz frequency bandwidth. Note the East-West velocity gradient across the San Andreas Fault and the U-shaped low-velocity region around 2.5 km below the surface. The white dots at the surface refer to the station locations.

frequency, the inversion produced a residual variance reduction around 50% relative to the residuals for the homogeneous model (see Figure S1 of the auxiliary material).[1] Note that the same group velocity inversion performed without the ORA procedure lead to strongly biased results (see Figure S2).

3. Three-Dimensional Shear-Wave Velocity Inversion

[11] From each cell of the model, we extracted the frequency-dependent group velocities for the Love waves, obtaining one dispersion curve per grid cell (see Figure S3, right). The dispersion curves reconstructed for every cell were then inverted, to obtain the corresponding 1-D depth-dependent shear-velocity profiles. To correctly image the shallow structure of the SAF, we used a simple five-layer parameterisation.

[12] The fitting procedure between the data and a five-sediment-layer forward model was carried out using an improved version of the Neighbourhood Algorithm (NA) [*Wathelet*, 2008]. In contrast to a basic Monte Carlo sampling, the NA attempts to guide the random generation of new samples by the results obtained on the previous samples. Voronoi cells are used to model the cost functions across the parameter space. As compared to a classical NA [*Sambridge*, 1999], this improved version better explored the non-uniqueness of the problem, thanks to continuous scaling of the parameter space. In the inversion process, the parameters that were allowed to vary were layer depths, and S-wave velocities. For each cell, the NA is stopped when 2,000 acceptable models (i.e., that fit the data within 10% of the lowest misfit error) are obtained. Such NA procedure usually generates a total of 10,000 to 60,000 models. For each cell, the final shear-wave velocity profile is the average of these 2,000 models (see Figure S3).

[13] Figure 3 shows the 3-D map of the shear-wave velocity around the SAF down to a depth of 3 km. The East-West velocity gradient across the SAF is clearly visible, as well as the low-velocity region down to ~2.5 km below the surface between the SAFOD hole and the SAF surface trace.

4. Discussion

[14] This U-shaped local structure has been imaged in several studies using P-wave and S-wave tomography based on refraction/reflection seismic experiments [*Catchings et al.*, 2002; *Bleibinhaus et al.*, 2007; *Hole et al.*, 2006] and local earthquake arrival times [*Roecker et al.*, 2006; *Thurber et al.*, 2004]. The first method here creates by definition a 2-D image of P-wave velocity across the SAF at the SAFOD drilling site (see Figure S4). The second method should provide a 3-D image of the area for both the P-waves and S-waves, as the earthquake epicentres were located along ~15 km of the SAF, although only two sections across the SAF were shown in *Roecker et al.* 2006. Obviously, these two inversion results do not have the same resolution, as they did not share the same objective up front. The seismic refraction study was aimed at observing the geological structure of the area to a 15-km distance on each side of the SAF, with local resolution at depths obtained by tuning up the frequency content of the inversion. On the other hand, the P-wave and S-wave tomography inversions provided by local earthquakes only provided high resolution at the fault zone. Despite qualitative agreement on the local shape of the geological structure at the SAF, it is then not surprising to observe discrepancies on P-wave velocities between these two studies. For example, with the seismic refraction study, note the higher velocities (5.5–6.5 km/s) obtained west of the SAF, within 1.5 km of the surface, which were themselves in agreement with P-wave inversion results obtained on the SAF a short distance north of Parkfield [*Ben-Zion and Malin*, 1991; *Lewis et al.*, 2007].

[15] It is then difficult to make any quantitative comparison with the S-wave velocity 3-D pictures obtained in the present study with ANSWT (Figure 3). The main interest of our study lay in the 3-D velocity contour (Figure 4) around the SAF fault that showed a 1.3-km wide steep dipping, and nearly vertical geological structures between the Salinian granite (south-west) and the Franciscan sedimentary rocks (north-east). Indeed, many studies agree that there is a steep wedge of low seismic velocity between Salinia and the SAF in the uppermost crust. This structure might be related to the presence of several major faults in the vicinity of the SAF in Parkfield (namely, the Buzzard Canyon Fault and Gold Hill Fault [*Hole et al.*, 2006]). As indicated by steep-dip migration

[1] Auxiliary materials are available in the HTML. doi:10.1029/2011GL047811.

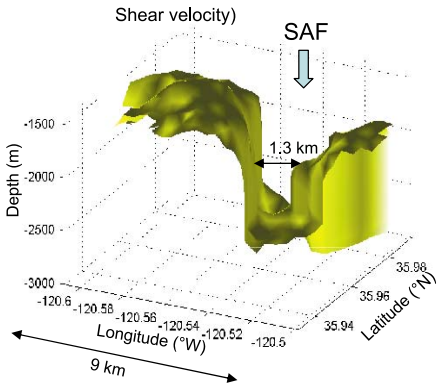

Figure 4. Three-dimensional iso-velocity contour at 2.5 km/s in the alignment of the San Andreas Fault showing the steep dipping (the Buzzard Canyon Fault) on the west side and an oblique thrust fault (the Gold Hill Fault) on the east side. The SAF location is shown as a blue arrow.

obtained from a reflection seismic study [*Bleibinhaus et al.*, 2007], Gold Hill Fault is a moderately dipping (oblique) thrust fault near Parkfield, although it might be very steep below the surface. Interestingly enough, the locations of the local earthquakes corresponded to the dip in the SAF [*Thurber et al.*, 2004], with the shallowest earthquakes approximately 2.5 km to 2.7 km below the surface at or near the base of this wedge.

[16] The tomography inversions in Figures 3 and 4 resulted from the combination of 360 selected dispersion curves for Love waves extracted from 15 days of ambient seismic noise. As the number of cross-correlation pairs (i.e., the number of ray paths) increased as the square of the number of stations, the spatial resolution of seismic noise tomography maps can be improved easily. If more stations are installed as a temporary seismic network in Parkfield, the contributions of seismic-noise tomography might become relevant to our understanding of the shallow structural relationships between the SAF, the Gold Hill Fault, the Buzzard Canyon Fault, and the faulted edge of Salinia.

[17] **Acknowledgments.** The facilities of the IRIS Data Management System were used for access to the waveforms and metadata required in this study. U.S. Geological Survey and New Mexico Bureau of Mines and Mineral Resources, 2006, Quaternary fault and fold database for the United States, was accessed Mar 31, 2011, from USGS web site.

[18] The Editor thanks two anonymous reviewers for their assistance in evaluating this paper.

References

Barmin, M. P., M. H. Ritzwoller, and A. L. Levshin (2001), A fast and reliable method for surface wave tomography, *Pure Appl. Geophys.*, *158*, 1351–1375, doi:10.1007/PL00001225.

Bensen, G. D., M. H. Ritzwoller, M. P. Barmin, A. L. Levshin, F. Lin, M. P. Moschetti, N. M. Shapiro, and Y. Yang (2007), Processing seismic ambient noise data to obtain broad-band surface-wave-dispersion measurements, *Geophys. J. Int.*, *169*, 1239–1260, doi:10.1111/j.1365-246X.2007.03374.x.

Ben-Zion, Y., and P. Malin (1991), San Andreas Fault zone head waves near Parkfield, California, *Science*, *251*, 1592–1594, doi:10.1126/science.251.5001.1592.

Bleibinhaus, F., J. A. Hole, T. Ryberg, and G. S. Fuis (2007), Structure of the California Coast Ranges and San Andreas Fault at SAFOD from seismic waveform inversion and reflection imaging, *J. Geophys. Res.*, *112*, B06315, doi:10.1029/2006JB004611.

Catchings, R. D., M. J. Rymer, M. R. Goldman, J. A. Hole, R. Huggins, and C. Lippus (2002), High resolution seismic velocities and shallow structure of the San Andreas Fault zone at Middle Mountain, Parkfield, California, *Bull. Seismol. Soc. Am.*, *92*, 2493–2503, doi:10.1785/0120010263.

Ekström, G., J. Trömp, and E. W. F. Larson (1997), Measurements and global models of surface wave propagation, *J. Geophys. Res.*, *102*, 8137–8157, doi:10.1029/96JB03729.

Froment, B., M. Campillo, P. Roux, P. Gouedard, A. Verdel, and R. L. Weaver (2010), Estimation of the effect of non-isotropically distributed energy on the apparent arrival time in correlations, *Geophysics*, *75*, SA85–SA93, doi:10.1190/1.3483102.

Hole, J. A., T. Ryberg, G. S. Fuis, F. Bleibinhaus, and A. K. Sharma (2006), Structure of the San Andreas Fault zone at SAFOD from a seismic refraction survey, *Geophys. Res. Lett.*, *33*, L07312, doi:10.1029/2005GL025194.

Lewis, M. A., Y. Ben-Zion, and J. J. McGuire (2007), Imaging the deep structure of the San Andreas Fault south of Hollister with joint analysis of fault zone head and direct P arrivals, *Geophys. J. Int.*, *169*, 1028–1042, doi:10.1111/j.1365-246X.2006.03319.x.

Li, Y.-G., J. E. Vidale, and E. S. Cochran (2004), Low-velocity damaged structure of the San Andreas Fault at Parkfield from fault zone trapped waves, *Geophys. Res. Lett.*, *31*, L12S06, doi:10.1029/2003GL019044.

Moschetti, M. P., M. H. Ritzwoller, and N. M. Shapiro (2007), Surface wave tomography of the western United States from ambient seismic noise: Rayleigh wave group velocity maps, *Geochem. Geophys. Geosyst.*, *8*, Q08010, doi:10.1029/2007GC001655.

Roecker, S., C. Thurber, K. Roberts, and L. Powell (2006), Refining the image of the San Andreas Fault near Parkfield, California using a finite difference travel time computation technique, *Tectonophysics*, *426*, 189–205, doi:10.1016/j.tecto.2006.02.026.

Roueff, A., P. Roux, and P. Réfrégier (2009), Wave separation in ambient seismic noise using intrinsic coherence and polarization filtering, *Signal Process.*, *89*, 410–421, doi:10.1016/j.sigpro.2008.09.008.

Roux, P. (2009), Passive seismic imaging with directive ambient noise: application to surface waves and the San Andreas Fault in Parkfield, CA, *Geophys. J. Int.*, *179*, 367–373, doi:10.1111/j.1365-246X.2009.04282.x.

Roux, P., K. G. Sabra, P. Gerstoft, and W. A. Kuperman (2005), P-waves from cross-correlation of seismic ambient noise, *Geophys. Res. Lett.*, *32*, L19303, doi:10.1029/2005GL023803.

Sabra, K. G., P. Gerstoft, P. Roux, W. A. Kuperman, and M. C. Fehler (2005), Surface-wave tomography from microseisms in southern California, *Geophys. Res. Lett.*, *32*, L14311, doi:10.1029/2005GL023155.

Sambridge, M. (1999), Geophysical inversion with a neighbourhood algorithm: I. Searching a parameter space, *Geophys. J. Int.*, *138*, 479–494, doi:10.1046/j.1365-246X.1999.00876.x.

Shapiro, N. M., M. Campillo, L. Stehly, and M. H. Ritzwoller (2005), High resolution surface wave tomography from ambient seismic noise, *Science*, *307*, 1615–1618, doi:10.1126/science.1108339.

Stehly, L., B. Fry, M. Campillo, N. M. Shapiro, J. Guilbert, L. Boschi, and D. Giardini (2009), Tomography of the Alpine region from observations of seismic ambient noise, *Geophys. J. Int.*, *178*, 338–350, doi:10.1111/j.1365-246X.2009.04132.x.

Tanimoto, T., S. Ishimaru, and C. Alvizuri (2006), Seasonality in particle motion of microseisms, *Geophys. J. Int.*, *166*, 253–266, doi:10.1111/j.1365-246X.2006.02931.x.

Thurber, C., S. Roecker, H. Zhang, S. Baher, and W. Ellsworth (2004), Fine-scale structure of the San Andreas Fault zone and location of the SAFOD target earthquakes, *Geophys. Res. Lett.*, *31*, L12S02, doi:10.1029/2003GL019398.

Waldhauser, F., E. Kissling, J. Ansorge, and S. Mueller (1998), Three-dimensional interface modelling with two-dimensional seismic data: The Alpine crust mantle boundary, *Geophys. J. Int.*, *135*, 264–278, doi:10.1046/j.1365-246X.1998.00647.x.

Wathelet, M. (2008), An improved neighbourhood algorithm: Parameter conditions and dynamic scaling, *Geophys. Res. Lett.*, *35*, L09301, doi:10.1029/2008GL033256.

Yang, Y., M. H. Ritzwoller, A. L. Levshin, and N. M. Shapiro (2007), Ambient noise Rayleigh wave tomography across Europe, *Geophys. J. Int.*, *168*, 259–274, doi:10.1111/j.1365-246X.2006.03203.x.

Yao, H., and R. D. Van der Hilst (2009), Analysis of ambient noise energy distribution and phase velocity bias in ambient noise tomography, with application to SE Tibet, *Geophys. J. Int.*, *179*, 1113–1132, doi:10.1111/j.1365-246X.2009.04329.x.

A. Roueff, Institut Fresnel, CNRS, Aix-Marseille Université, Ecole Centrale Marseille, Campus de Saint Jérôme, F-13013 Marseille CEDEX, France.

P. Roux and M. Wathelet, ISTerre, CNRS, IRD, Université Joseph Fourier, Maison des Géosciences, 1381 rue de la Piscine, BP 53, F-38041 Grenoble CEDEX 9, France. (philippe.roux@obs.ujf-grenoble.fr)